Multi-resolution X-ray imaging techniques for bulk operational applications: A short review and a proposed streamlined workflow

Naif J. Alqahtani [*], *Sinan Caliskan*, *Tariq A. Almubarak, & Sultan M. Alenizi*

[1]EXPEC Advanced Research Centre, Saudi Aramco, 31311 Dhahran, Saudi Arabia

Abstract. X-ray imaging is a widely used non-invasive technique for characterizing core materials from reservoirs in Petroleum engineering. Different scales of X-ray imaging, such as Medical Computed Tomography (CT), Micro-CT, and Nano-CT, can reveal various features of the core, such as integrity, fractures, fossils, mud invasion, pore morphology, clay presence, and fluid displacement. However, for industrial applications that involve processing large amounts of core footage from coring operations, there is no systematic method for selecting representative samples for further advanced testing, such as special core analysis (SCAL) or comprehensive digital rock analysis. In this paper, we review all previously mentioned X-ray imaging techniques and their use in industrial applications. Further, we propose a workflow and a systematic method for optimizing the use of the limited X-ray resources to obtain a comprehensive multi-scale analysis of the core materials. This workflow aims to streamline the X-ray imaging processes of the core footage and enhance the quality and efficiency of the data acquisition and analysis.

1. Introduction

The journey of core extraction and analysis from the subsurface during drilling operations for formation evaluation is an intricate process. The extracted core goes through multiple stages of wellbore retrieval, handling, inspection, preservation, and analysis [1,2]. Coring and core analysis are among the most direct methods for evaluating formations and often require a considerable investment when drilling exploration and development wells. Thus, it is of utmost importance to fully exploit all resources to extract the most information from the recovered cores [1–3].

Coring involves drilling into a well and extracting a cylindrical sample, known as a 'core'. This core is a physical representation of the subsurface layers, providing direct information about the geological formation. It reveals the rock's mineral composition, structural features, and the presence of hydrocarbons [2,4]. Core analysis, therefore, is a critical step in reservoir characterization. It involves laboratory tests to measure properties such as porosity (the volume of void space within the rock), permeability (the ability of fluids to flow through the rock), and fluid saturation. These parameters are essential for reservoir modeling and predicting its performance [2,3,5].

The use of X-ray imaging in core analysis provides a non-destructive method to visualize and analyze the internal structure of core samples [6–8] This technique allows scientists across multiple scales to examine and infer many petrophysical properties of the rock without physically altering or damaging the sample [9–11]. For example, aluminum core barrels used to preserve whole core samples can be easily and effectively imaged using medical CT without the need to open the core barrels revealing many insights about the core status in terms of damage that might be induced by drilling operations (mud invasion), or retrieval and transportation (i.e. fractures and breakage) [9,12,13].

Multi-scale X-ray imaging, which includes Medical CT, Micro-CT, and Nano-CT, has further enhanced our ability to analyze core materials at various scales, from whole core to core plugs, cuttings, and rock fragments[8,14,15]. These techniques have opened new avenues for understanding the complex structures and physical phenomena of reservoir rocks and their dynamics, each with its unique advantages and applications [16,17]. The choice of technique depends on the scale of interest and the specific technical question, making multi-scale X-ray imaging a versatile tool in core analysis. In Figure 1, a comparison between the spatial resolution and sample size is depicted for different common methods of imaging, and in Figure 2, we show a typical pore size distribution of carbonate rock obtained from a mercury intrusion experiment to show the different scales at which porosity exists. Carbonate rocks often exhibit multiple pore systems ranging in size from caverns (meters) down to nanopores systems [18–20].

While these techniques can indeed support and complement many findings about reservoirs from other sources such as logs and analytical core experiments, they also can be utilized to be the sole source of many preliminary findings about subsurface formations[21–23]. Hence, it is essential to select representative samples of the dominant rock types existing in a formation whenever going downscale [21].

In this paper, we review the use of multi-resolution X-ray CT scanners, namely Medical CT, Micro-CT, and Nano-CT, to

[*] Corresponding author: Naif.Alqahtani.3@aramco.com

visualize and characterize rocks, with emphasis on the use in industrial applications for bulk core analysis. We also delve into each method's applications and limitations with many examples and case studies from the literature and our experiments. We finally propose a workflow that enables a systematic sample selection for further investigation whenever a core analysis objective needs to be met with a finer resolution X-ray imaging.

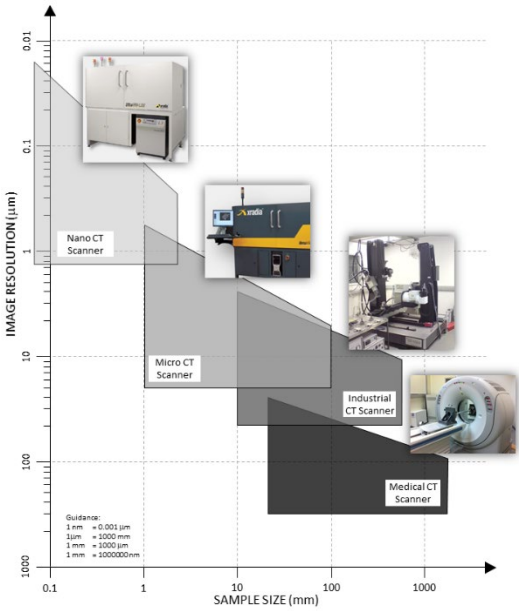

Fig. 1. Comparison of approximate image resolution and sample sizes for different types of X-ray CT scanners.

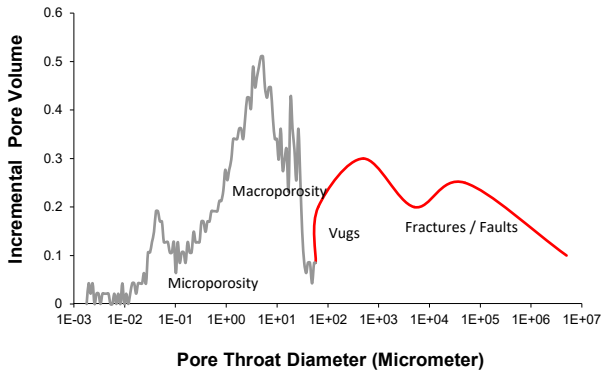

Fig. 2. A typical pore size distribution of Carbonate rock (Indiana Limestone) obtained from mercury intrusion test (grey line). The red line shows theoretical pore size distribution at larger scales.

2. Medical CT

Since the early 1980s, X-ray computerized tomography (CT) scanning has been successfully used as a powerful non-destructive, non-invasive research tool in geoscience to examine whole cores as well as smaller rock samples for various purposes, e.g. core characterization, whole core inspection within their protective barrels, sample selection, damage/fracture detection, mud invasion and so forth [9,24,25]. More advanced applications, such as porosity and determination[26], displaying damages and wormholes[27] in 3D mode due to fluid injection tests as well as displaying fluid flow movement within rock samples have now been routinely undertaken [28]. Furthermore, micro-CT scanners, which we give more details about in section 3, equipped with in-situ testing capabilities, such as geomechanical apparatus [29]and high-resolution region of interest imaging of shale samples for unconventional resources [30] have provided further insights - in the oil and gas laboratories.

Medical and industrial type CT scanners (including micro- and nano-CT scanners) all share the basic principles of the X-ray CT technique to visualize the internal structures of objects in a non-destructive manner, i.e. all the CT systems have an X-ray tube and on the opposite side is the detectors whilst the scanning performed the object is positioned between them. The X-rays transmitted through the object are attenuated and captured by the detectors. When a rock sample is CT scanned (see Figure 3), focused and collimated beams from an X-ray source penetrate and travel through the sample, and the attenuated beams are recorded by detectors. Energy attenuation is related to the electron density and effective atomic number of the mineralogy of the sample being scanned. Each material has a distinct linear attenuation coefficient and hence the total response received by the detectors is a combination of these coefficients. Dual-energy CT scanning, on the other hand, involves the same sample being scanned at two different X-ray energy levels. Wellington and Vinegar [6] stated that one scanning provides CT images proportional only to the bulk density at a high X-ray energy scan (higher than 100 kV), and the low X-ray energy (lower than 100 kV) scan is proportional to atomic number. In the case of fluid flow visualization, however, in addition to the use of all aspects of CT scanning features, radiopaque traces (dopants) are also needed to be able to monitor the fluid movement inside the cores during the core flooding. The role of the dopants is essentially to provide adequate contrast between various phases to view and analyze the saturation distribution during the scanning [26,31,32].

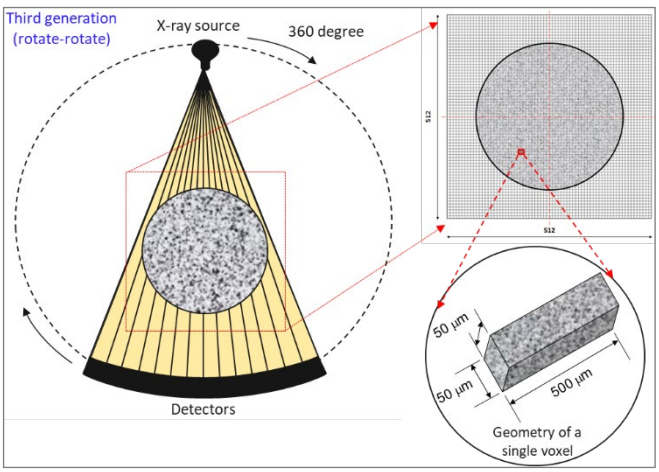

Fig. 3. A representation of a rock sample within a medical-type CT scanner.

In Figure 4, an example of the use of Medical CT scanners is presented where 3-foot whole core barrels are scanned at 100

kV. The scans show poorly recovered or damaged samples on the left and good sample recovery on the right. Also, lamination and inclined beddings at an angle of about 30 degrees can be observed on the sample on the right.

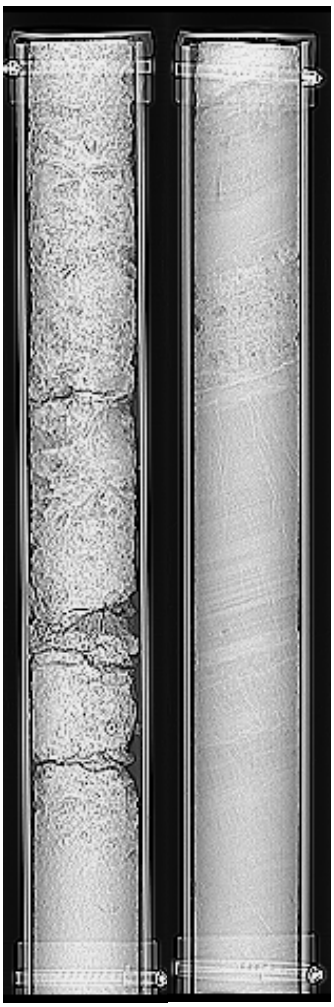

Fig. 4. Two pilot scans of whole core samples placed in 3-foot aluminium barrels. The left sample is an example of a poorly recovered sample or damaged sample. In contrast, the one on the right shows good recovery with an indication of inclined formation bedding and lamination.

Another important application of the medical CT type of scanners is the ability to determine the approximate density of the material by linking it to the average CT numbers at a given depth. In Figure 5, a quick demonstration shows CT can determine low-density sections in the whole core (see green section in the heatmap corresponding to density) which could be an indication of more porous rock.

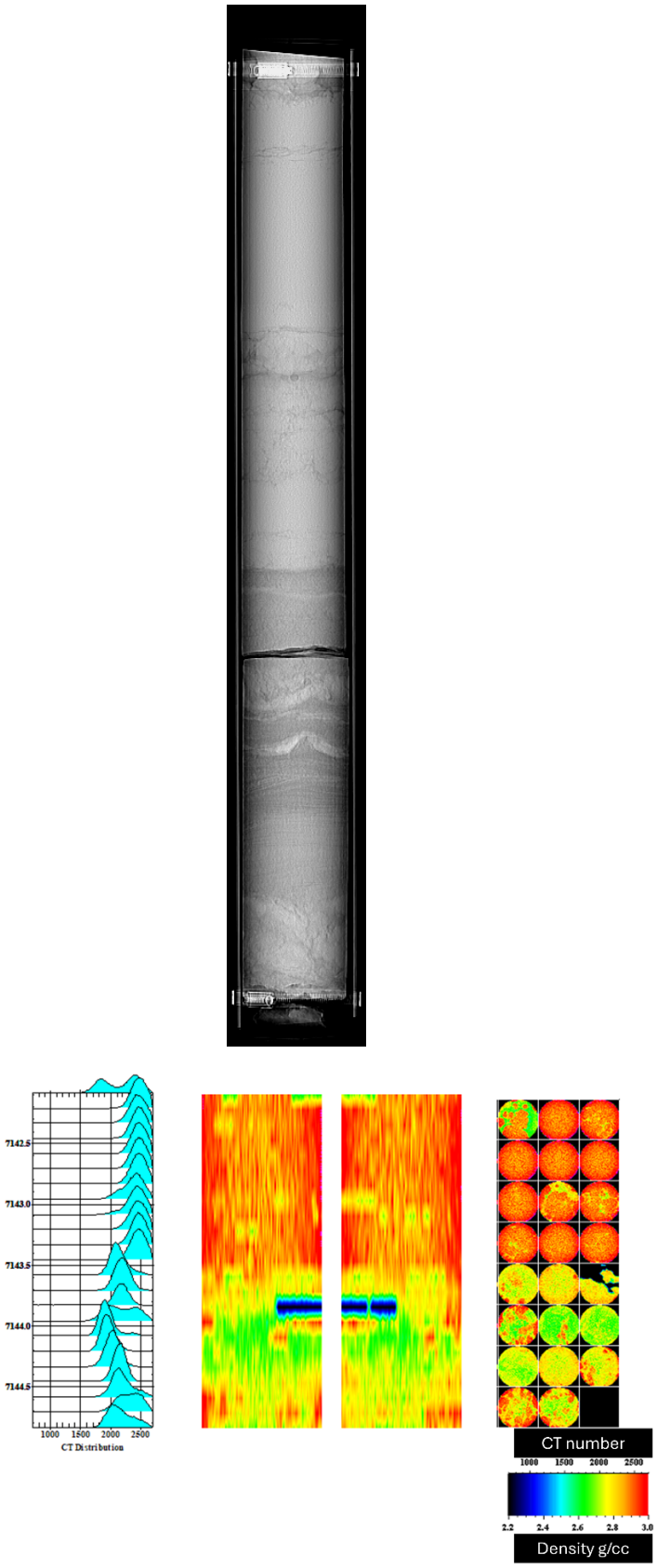

Fig. 5. (upper) A 3-foot whole core section pilot scan with (lower) corresponding average CT number across the depth of the core sample, heatmap corresponding to relative density, and cross-sectional slices taken every 5 mm. The blue section in the heatmap corresponds to the breakage/fracture in the whole core and the green section to lower-density rock types.

The main difference between these major types of CT scanners is the purpose, for which they were designed. This design difference dictates some differences that influence their performance in their uses for various purposes (see a summary of comparison in Table 1). Medical-type CT scanners typically have a 512x512 matrix that yields pixel sizes ranging approximately from 50 to 400 mm depending on the object size being scanned. Since the medical type of CT scanners is designed with humans in mind, they have apparent disadvantages in nonmedical applications, e.g. geological and petroleum engineering with smaller samples, i.e. typically smaller than 1.5 inches in diameter. Another apparent disadvantage of using the medical type of CT scanner is their limited X-ray power, i.e. usually they are limited to 140 kV. This means that high-density and larger samples, such as rocks or ceramics larger than 100 mm diameter may face problems since the X-ray beams of the medical type of CT scanners may be inadequate to penetrate.

Current CT systems have significantly improved features in hardware and software over the decades including the cooling efficiency of the X-ray tubes, number of slices per rotation, advanced features of the control software, etc. However, slice thickness has relatively remained unchanged having the typical slice thickness of 0.5 mm. An Increased number of slices per rotation means, that modern-day CT scanners have more rows of detectors, which means that these scanners can cover larger volumes per scanning, yielding higher efficiency in CT scanning practices and higher image resolution. The typical size of the matrix of conventional CT scanners has always been 512x512 pixels. However, it is now easier to find scanners with the capability of 1024x1024 or even 2048x2048 matrix sizes, which influence the image quality to a great extent (See Table 2). In addition to the CT scanner type, the image quality is also influenced to a great extent as a function of sample size, which is highlighted earlier in Figure 1.

Table 1. Comparison of typical parameters of medical and industrial type CT scanners.

Parameters	**Medical CT**	**Industrial CT (Micro and Nano CT scanners)**
Resolution	50 - 400 µm voxel size	0.00015 - 50 µm voxel size
Scan time (per sample)	~ 30 seconds to 5 minutes	~ A few minutes – more than 24 H
X-ray tubes and detectors	They are locked in their position to rotate together around an object during scanning	Often sample position is set before scanning and it remains in stationary condition throughout the scanning. Some models rotate only the source and detector during scanning.
Sample size	25 - 2000 mm length, 25 – 700 mm diameter (for hard materials, such as rocks, the diameter is usually limited to 100 mm)	<1 - 100 mm length, <1 – 200 mm diameter (only custom-built industrial scanners accommodate longer samples) Nano CT: max object size 100 – 200 µm
X-ray voltage	80 - 140 kV	Up to 450 kV
Allowed dosage	Limited (prescribed based on patient)	No limit
Radiation protection	External protection is required. (lead shielding in all walls)	Self-shielding (scanner is lead insulated)
Sample condition during scanning	Stationary (short-axial) or moves horizontally (scout, long-axial and helical)	Often the sample is rotated around its center and vertical movement is allowed during scanning. Some models allow the sample to be stationary and rotate the source and detectors around the sample.
Object	Designed for the human body (successfully used for other objects, e.g. ceramics, concrete, rock, wood products, etc.)	Designed for industrial applications, objects vary widely (metals, plants, composites, rock samples, plastics, etc.)
Operation	Basic training and experience could be adequate	A thorough understanding and an advanced level of training are essential.
Access to internal hardware	Limited access (employing control software only)	Flexible access (internal hardware visible) (extra caution is required)

Table 2 Theoretical sizes of one pixel (mm) according to matrix size and reconstruction field of view (FOV).

Matrix size			512x512	1024x1024	2048x2048
Image size (FOV)	30 mm	Size of one pixel (mm)	0.059	0.029	0.015
	40 mm		0.078	0.039	0.02
	100 mm		0.195	0.098	0.049
	120 mm		0.234	0.117	0.059
	140 mm		0.273	0.137	0.068
	200 mm		0.391	0.195	0.098
	300 mm		0.586	0.293	0.146

3. Micro CT

Micro-CT imaging, with its ability to provide a finer scale resolution, enables the examination of rocks down to a voxel size of one micrometer or less [10,33,34]. This technology proves particularly effective in the study of conventional reservoir sandstones and some carbonates where the majority of the pore space is resolved. The resolution offered by modern Micro-CT scanners is often sufficient to model and infer a wide range of petrophysical properties with satisfactory results [35].

These advanced micro-CT scanners can precisely determine the geometry and connectivity of the pore space, empowering scientists to often estimate physical properties with reasonable accuracy, such as porosity and specific surface area and phase topology solely through image analysis [36,37]. Furthermore, the simulation of fluid flow within the pore space is possible by solving governing equations like Navier-Stokes [11,38,39]. This allows for the estimation of various parameters including absolute and relative permeabilities, gas diffusion, and electrical conductivity, to mention a few [40–42]. This type of analysis is commonly referred to as Digital Rock Analysis (DRA), or Digital Rock Physics (DRP) [35,43–45]. DRA represents a swift and reproducible suite of methods for rock characterization. It facilitates the estimation of numerous petrophysical rock properties that would traditionally require time-consuming laboratory experiments, thereby enhancing efficiency in the field. Recent advancements in computer vision, deep learning, and simulation methods have further enhanced the accuracy and interpretation of DRA enabling scientists to get accurate answers for tighter rock with positively skewed pore size distribution [46,47].

Micro-CT raw image acquisition process begins with the emission of X-rays from a micro-CT X-ray tube, which are then attenuated as they pass through the sample, a phenomenon described by Beer's Law [48]. The attenuated X-rays are captured by a detector, creating 2D projection images. As the sample rotates, multiple 2D projections are obtained from different angles. These 2D projections are then reconstructed into a 3D volume using a variety of algorithms [49]. After creating a volume image, image processing and filtering techniques are applied to enhance the quality of the reconstructed images and remove imaging artifacts such as beam hardening and ring effects [50]. In Figure 6, we show an example of an acquisition process of a micro-CT image of an Indiana limestone sample. The 1-inch core plug shown is sub-plugged into a 4-millimeter mini-plug used for imaging, generating an image with a voxel size of 2.46 micrometer. It can be noticed that even with this limited sample size and field of view, not all pore spaces are resolved as many textures appear to have micro-porosity represented by dark grey textures. Yet, many techniques and methods have been developed to study, and quantify unresolved porosity and its effect on fluid flow, and electrical properties among many more [51–53].

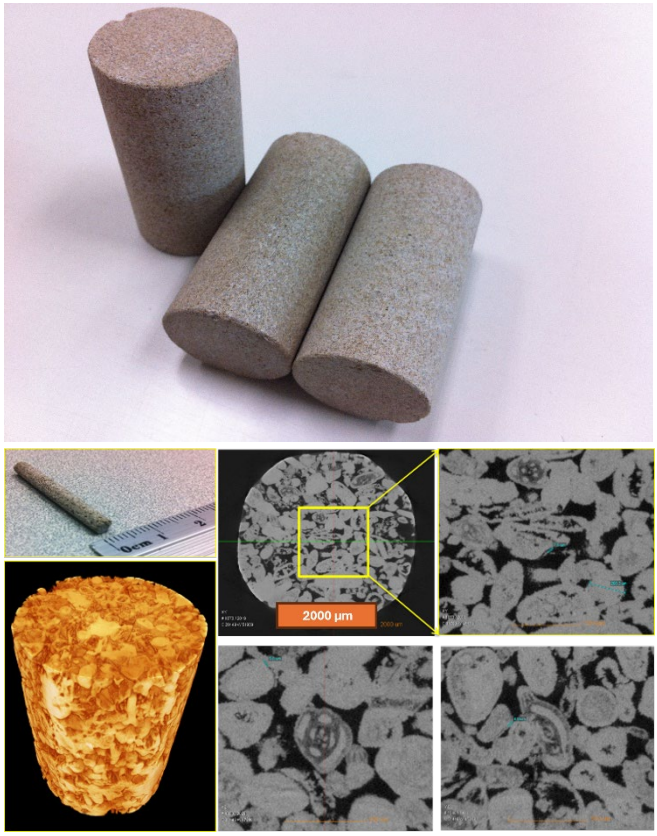

Fig. 6. (Upper) an Indiana limestone sample of 1-inch diameter. (Lower) a mini-plug taken from the 1-inch limestone core plug along with some cross-sectional visualization from the micro-CT image of the mini-plug and a 3D volume visualization. The zoomed-in region in the yellow square measures (1400 ×1400 µm). Pore space is black and limestone oolites (Carbonate grains) are bright grey. Unresolved microporosity appears as dark grey inside some oolites.

Many applications for micro-CT imaging have been documented in the literature. Phase quantification including pore space, fluids, and minerals phases can be directly computed from the images [35]. Geometrical and topological measurements of the existing phases can also be quantified or estimated (i.e. surface area, shape factor, Euler characteristic

number, coordination number, and tortuosity) [37]. Many researchers also showed methods for computing contacting angle and characterizing the wettability of samples via in-situ micro-CT imaging methods which are essential parameters in many reservoir engineering applications[54,55]. Finally, single and multi-phase flow, reactive transport, deformability, and geomechanical simulations provide many insights into answering technical questions about oil and gas production and recovery, CO2 capture and storage, and groundwater transport [53,56]. For example, Regaieg et. Al [46,47] presented methods for capturing accurate relative permeability curves using pore network modeling with an accurate assessment of wettability via laboratory experiments. In Figure 7 we show an exemplary use of micro-CT imaging and analysis after Higgs et. al [57] to compute the macroscopic contact angle of a hydrogen bubble inside a doped brine-saturated sample. The contact angle in the reference paper [57] is computed for multiple droplets along the contact line with grains which gives a range of contact angle shown in the histogram. The findings of this study show a similar contact angle to other experimental methods published in the literature [58]. This study and others that used X-ray CT imaging, support replacing parts of the time-consuming experimental SCAL work with CT imaging and modeling, especially, for sample screening and selection.

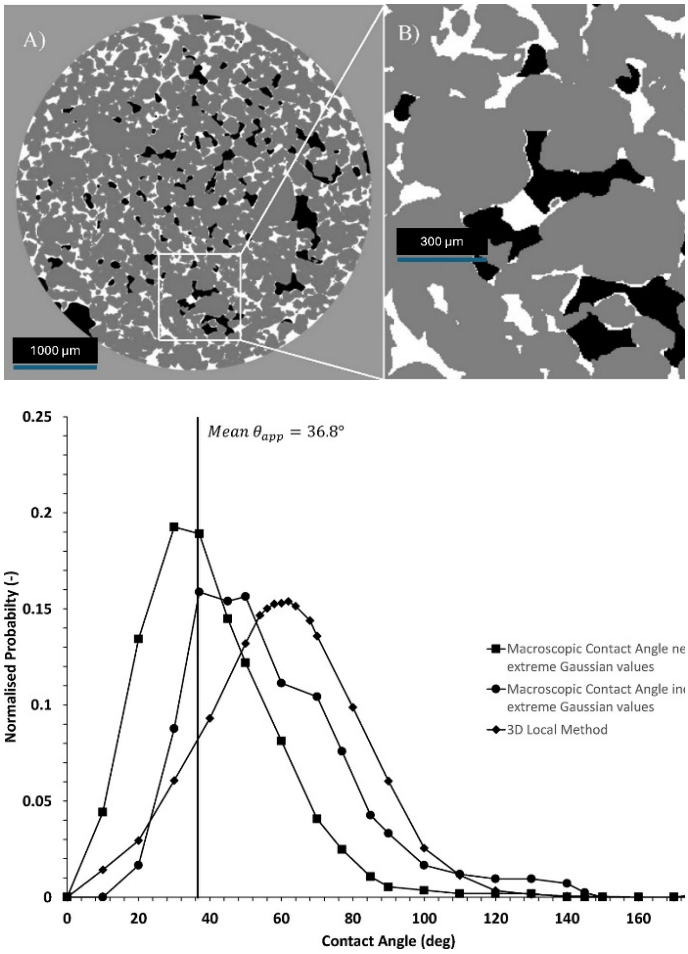

Fig. 7. (Upper) Segmented micro-CT image showing rock grains (dark gray), doped brine with KI (white), and hydrogen gas (black) used to estimate the contact angle of hydrogen blobs within brine. (Lower) the distribution of contact angles measured through multiple algorithms (after Higgs, et. Al [57]).

The advancement of imaging, processing, and modeling techniques made many enhancements to what can be achieved through DRP workflows. For example, the use of dopants to enhance the contrast between fluid(s) and grain phases is well documented in the literature [52]. These dopants can enhance differential imaging techniques where the sample can be imaged dry and saturated. The improvements include the better monitoring of saturation during coreflooding, and the estimation of unresolved porosity[52]. However, care must be considered when using dopants as they can alter wettability [59].

Also, images recently can be enhanced digitally through the use of deep learning super-resolution techniques to reach voxel resolution beyond the X-ray CT hardware limits[19,60]. This is especially useful to tackle the known trade-off between field of view and resolution. Deep learning techniques can also be utilized to estimate physical properties and velocity fields of fluid flow in porous media. A comprehensive review of deep learning applications in pore-scale modeling is provided in [61].

4. Nano CT

Nano CT is also a non-destructive form of ultrahigh-resolution X-ray imaging[15]. It is a technique that provides 3D images similar to micro-CT, however, the resolution is in the nanometer range [62]. It is heavily used for biomedical applications [63] and has emerging applications in other sectors such as the oil and gas industry. For rock analysis, it is often used with the aid of other techniques such as focused ion beam imaging. A comparison of the variety of ultra-resolution imaging techniques and their associated scale is seen in Figure 8.

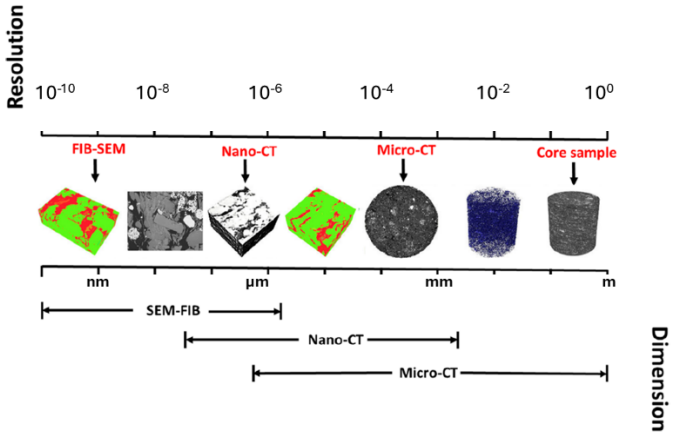

Fig. 8. A comparison between multiple ultra-resolution imaging techniques (after Garum[64]).

Nano-CT builds upon the same concept of micro-CT. It uses a transmission target X-ray tube and allows the focal spot size to be reduced to less than 500 nanometers. The equipment contains many detectors to achieve superior spatial resolution. Nano CT can provide resolutions down to 50 nanometers improving the ability to visualize internal pore structures and geometries with enhanced clarity [64].

This sophisticated tool can determine microstructures, porosity, and grain size distribution of ultra-tight rocks including shales, coal, and tight sands etc [62,64,65]. Additionally, by analyzing the X-ray attenuation patterns, it can differentiate between minerals such as calcite, and common, clays [66]. Moreover, it is able to reveal details about mineral phases, pore networks, and organic matter in the sample.

When comparing Nano-CT to FIB-SEM, we note that Nano-CT can work with much larger samples, provides clarity in material contrast, is much quicker in testing time, and generates 3D images easily. On the contrary, FIB-SEM provides a much higher resolution at the expense of longer testing duration, faces challenges in 3D imaging, and is destructive through milling the material during imaging. In Figure 9, we show an example from [67] study to characterize organic-rich shale fracture growth using a nano-CT. The study showed the stages at which the fracture grows and cut the sample into two halves. Such a study is important as it gives more insights into the pore space changes from a geomechanical perspective.

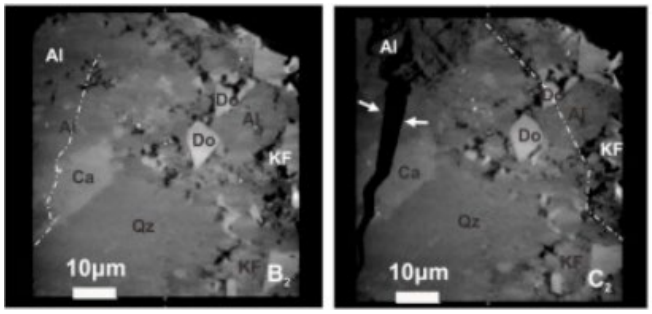

Fig. 9 Fracture growth study in organic shale conducted using a Nano-CT scanner (After Wu et. al. [67]).

Some of the downsides of using nano-CT include limited penetration depth. Nano CT is excellent for imaging thin samples but lacks the ability to image thicker samples due to the inability of the X-rays to fully penetrate the sample which leads to incomplete data acquisition. Additionally, artifacts can arise in the image due to a variety of reasons such as sample preparation conditions or beam hardening[68]. The tube power is also constrained by the voxel size and the high-resolution images can require higher user interaction during image analysis where balancing throughput and detailed imaging might be challenging. Moreover, sample preparation for nano CT imaging is not an easy task. It is an intricate and time-consuming process that requires proper handling and placing to avoid artifacts in the images [68]. As such, there has been limited research using Nano-CTs to study porous media and rocks as compared to the number of papers published on micro-CT imaging.

5. A suggested streamlined workflow for the effective utilization of multi-scale X-ray resources.

This section of the paper is intended to provide a general guideline for the effective use of X-ray imaging resources to aid in core analysis programs. While there are clear gaps in terms of the spatial resolution across the aftermentioned scanning methods of X-ray imaging, this discussion will be directed towards having the most of each scanning technique with the aid of other experimental core analysis, as this is a common practice in the oil and gas industry.

After the core extraction from a targeted formation, the core is often cut into 3-foot core segments and transported in aluminum barrels to the laboratory for further testing. In many cases, CT scanning is performed through only pilot longitudinal imaging in a single energy scanning mode in routine jobs. However, Dual Energy CT (DECT) scanning has been proven preferable not only in the acquisition of less noisy images but also to provide many insights that help estimate the density and porosity of the core. Siddiqui [21,22,26] provided a detailed description of the calculation of the effective atomic number (Z_{eff}) and apparent density which helps to correct the depths of the core as compared to depths from logs. It also provides a quick assessment of the variability of rock types within the cored section as shown in Figure 10 which can be achieved through many methods (i.e. texture, unsupervised machine learning, or statistically) [69–71]. Pilot images should provide a quick outlook on the status of the recovered core in terms of damage and mud invasion. Lastly, the CT scans can be used to decide the best parts to take core Routine or SCAL plugs from with the aid of other logs and lithological descriptions as shown in Figure 11 for a section of dolomitic formation. Preliminary classification of rock types based on imaging and comparison with laboratory experiments showed porosity ranking from best to worst [D, C, E, B, A] and permeability ranking [D, E, C, B, A]. One could perhaps link this ranking visually to the rock types according to the level of darkness or levels of CT number since these are mainly calcite except for rock type E which bears some anhydrite (see white stripes).

After plugging the core plugs out of the whole core, it can be scanned using the medical see to assess its homogeneity. Then the heterogeneity of the sample can be assessed either visually or quantitatively. For example, Maas et. Al. [71] has described a method for correlating the permeability variations of core plugs with the statics and the standard deviation of the Hounsfield units of raw tomographs of the core plugs. This enables qualifying samples with low deviations below a certain threshold for further analysis. Quick core plug tests such as single-phase flow permeability measurement, T1 and T2 NMR tests, and air porosity and permeability can easily aid in creating the final rock typing of the cored section. Such methods create metrics such as Flow Zone Indicators (FZI) and RQI to classify rocks and have been discussed in many publications including the following [23,72].

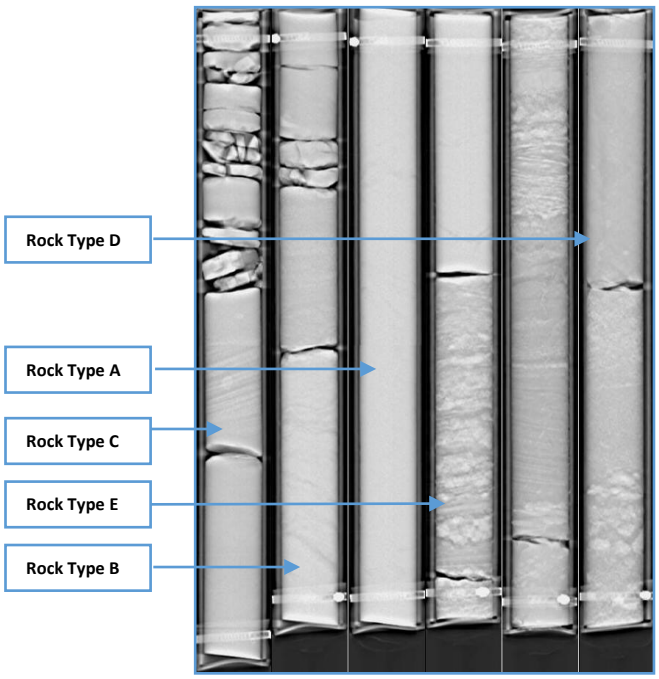

Fig. 10. A pilot longitudinal cross section showing different rock types of cores. This is often decided using multiple sources of data besides the core itself including wellbore logs, core gamma, and drill cuttings.

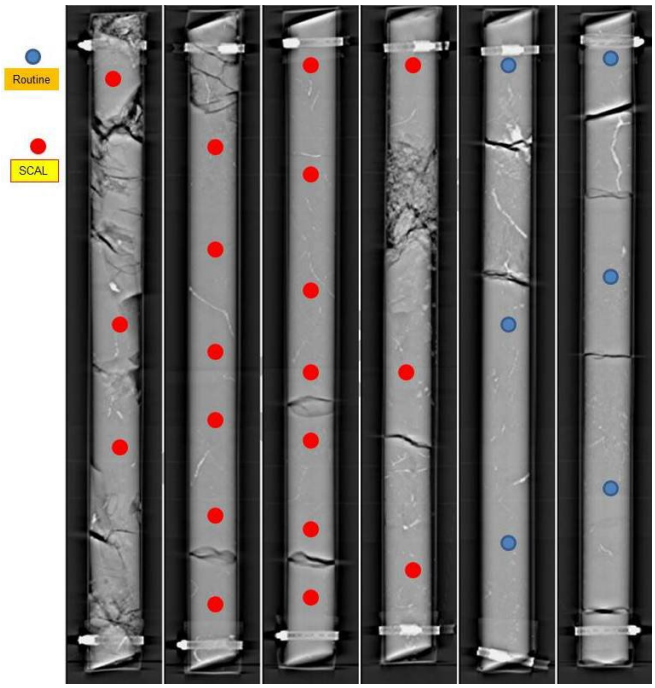

Fig. 11. An example of medical CT utilization for choosing samples for conventional and special core analysis.

The core plugs determined to be dominant rock types can be further studied using Micro- and Nano-CT scanners. Often a smaller plug sample is extracted to carry out the imaging to get a high-resolution image of the pore space. Here, it's important to carry out a full analysis of the Representative Elementary Volume required to carry out the targeted DRA accurately. This can be achieved through multiple methods including the following [73,74]. The determination of REV as illustrated in Figure 12 will eliminate the possibility of under-sampling from the subject image domain. It's also recommended to consider multiple locations having the same rock type to increase the statistical confidence in the obtained results.

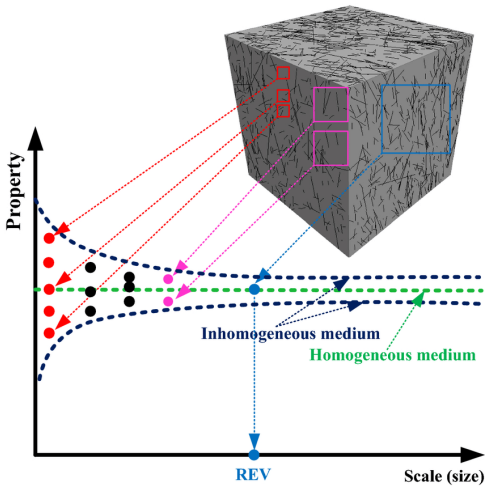

Fig. 12. An illustration of the variability of physical medium properties with domain size. At the REV, the variability of the property is minimal across the entire domain (After Wang [75]).

resolution methods of imaging can also help obtain more robust results, for example, QEMSCAM and SEM-EDS images can be registered to the 3D tomogram for better segmentation and image analysis [76]. Lastly, the results from multi-phase fluid simulation should be compared with experimental results to validate and adjust common simulation parameters (i.e. wettability, contact angle, fluids viscosities, etc.).

A workflow is presented in Figure 13 to summarize all the steps mentioned in this section which is commonly applied to process large volumes of core extracted. The workflow aims to exploit the X-ray scanner as much as possible to cover the dominant rock types seen often in reservoirs. This is meant for the routine core analysis programs and of course, the workflow can be adjusted to meet other analysis objectives.

While the timeline of the coring program often depends on the objective of the study and the level of detail required, the proposed process generally involves longer scanning time but occludes much of the testing time required for sample screening through laboratory experiments, especially core plugs. SCAL core plug sample screening often involves NMR T2 response measurement, brine permeability, air porosity, and permeability. This workflow has the potential to screen out many of the non-representative samples often set on the extreme ends of reservoir heterogeneities and its potential to proceed with SCAL testing. The process also can potentially yield significant cost savings as many core plug samples are omitted from laboratory testing.

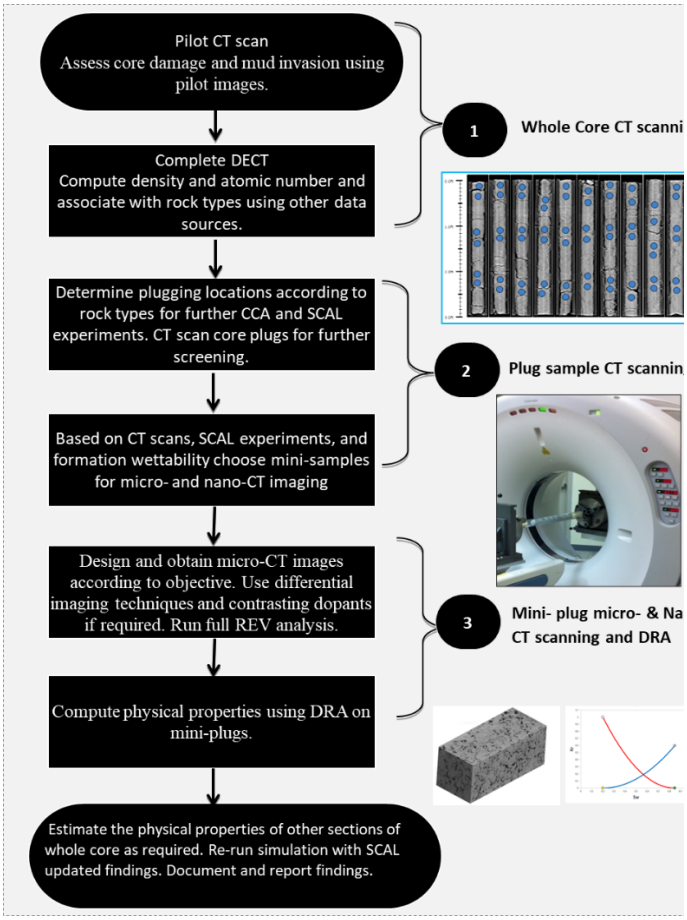

Fig. 13. A proposed workflow for the effective utilization of multi-scale X-ray resources for bulk coring analysis.

5. Summary

Coring operations and core analysis programs need ample budget and planning to fully reach their objective of formation evaluation. Although core analysis might seem like a minor operation, the reality is that it requires higher cost, time, and expertise to reach an accurate analysis. Thus, it's significantly important to plan for testing and utilize resources effectively, including X-ray imaging techniques. In this paper, we reviewed commonly available imaging techniques, theories, applications, and limitations. We also discussed how such imaging techniques can help with the success of core analysis programs. Finally, we proposed a comprehensive workflow to fully utilize X-ray imaging resources for reservoir description and characterization. This workflow tries to address geological and petrophysical observations from different scales separately, as having a link between the different scales requires either super-resolving or upscaling techniques. Thus, while having a continuum reservoir model for describing reservoir and rock typing at the micro- or millimeter scale seems a bit difficult with current technological and computational capabilities, it seems reasonable to invest more efforts in studying strategies for upscaling rock types for better geological modeling and reservoir description.

References:

1. R. Ashena, R. Ashena, G. Thonhauser, and G. Thonhauser, (2018).

2. C. McPhee, J. Reed, and I. Zubizarreta, (2015).

3. G. E. Archie, Am Assoc Pet Geol Bull **34**, 943 (1950).

4. H.-P. Xie, T. Liu, M.-Z. Gao, L. Chen, H.-W. Zhou, Y. Ju, F. Gao, X.-B. Peng, X.-J. Li, R.-D. Peng, Y.-N. Gao, C. Li, Z.-Q. He, M.-Q. Yang, and Z.-Y. Zhao, Pet Sci **18**, 1840 (2021).

5. J. O. Amaefule, M. Altunbay, D. Tiab, D. G. Kersey, and D. K. Keelan, in *All Days* (SPE*, 1993*).

6. S. L. Wellington and H. J. Vinegar, Journal of Petroleum Technology **39**, 885 (1987).

7. R. A. Ketcham and W. D. Carlson, Comput Geosci **27**, 381 (2001).

8. D. Wildenschild and A. P. Sheppard, Adv Water Resour **51**, 217 (2013).

9. J. Funk, (2011).

10. M. J. Blunt, B. Bijeljic, H. Dong, O. Gharbi, S. Iglauer, P. Mostaghimi, A. Paluszny, and C. Pentland, Adv Water Resour **51**, 197 (2013).

11. P. Mostaghimi, M. J. Blunt, and B. Bijeljic, Math Geosci **45**, 103 (2013).

12. P. Aérens, C. Torres-Verdín, and N. Espinoza, Petrophysics - The SPWLA Journal of Formation Evaluation and Reservoir Description **64**, 448 (2023).

13. P. K. Hunt, P. Engler, and C. Bajsarowicz, Journal of Petroleum Technology **40**, 1203 (1988).

14. J. Noe-Nygaard, F. Engstrøm, T. I. Sølling, and S. Roth, SPE Journal **22**, 41 (2016).

15. X. Guo, Y. Shen, and S. He, J Nat Gas Sci Eng **27**, 1630 (2015).

16. Y. A. Alzahid, P. Mostaghimi, N. J. Alqahtani, C. Sun, X. Lu, and R. T. Armstrong, J Colloid Interface Sci **554**, 554 (2019).

17. J. Schmatz, J. L. Urai, S. Berg, and H. Ott, Geophys Res Lett **42**, 2189 (2015).

18. I. A. Mahaman Salifou, H. Zhang, I. O. Boukari, M. Harouna, and Z. Cai, J Pet Sci Eng **196**, 107700 (2021).

19. N. J. Alqahtani, Y. Niu, Y. Da Wang, T. Chung, Z. Lanetc, A. Zhuravljov, R. T. Armstrong, and P. Mostaghimi, Transp Porous Media **143**, 497 (2022).

20. I. A. Mahaman Salifou, H. Zhang, I. O. Boukari, M. Harouna, and Z. Cai, J Pet Sci Eng **196**, 107700 (2021).

21. S. Siddiqui, T. Okasha, J. J. Funk, and A. M. Al-Harbi, (2003).

22. S. Siddiqui, T. M. Okasha, J. J. Funk, and A. M. Al-Harbi, SPE Reservoir Evaluation & Engineering **9**, 647 (2006).

23. J. O. Amaefule, M. Altunbay, D. Tiab, D. G. Kersey, and D. K. Keelan, in *All Days* (SPE*, 1993*).

24. S. Caliskan and A. Shebatalhamd, in *Day 3 Wed, April 26, 2017* (SPE*, 2017*).

25. S. Zabler, A. Rack, I. Manke, K. Thermann, J. Tiedemann, N. Harthill, and H. Riesemeier, J Struct Geol (2008).

26. S. Siddiqui and A. A. Khamees, (2004).

27. S. Algarni, M. S. Aljawad, H. Al-Majid, S. Alajmei, A. Abdulraheem, and D. Al-Shehri, Rock Mech Rock Eng **57**, 219 (2024).

28. S. Ahmed, A. S. Hanamertani, W. Alameri, E. W. Al-Shalabi, and M. R. Hashmet, Geoenergy Science and Engineering **221**, 211349 (2023).

29. N. Tisato, Q. Zhao, and G. Grasselli, Seg Technical Program Expanded Abstracts (2016).

30. Y. Wang, Seg Technical Program Expanded Abstracts (2017).

31. S. Siddiqui, P. J. Hicks, and A. S. Grader, J Pet Sci Eng (1996).

32. M. Iovea, G. Oaie, C. Ricman, G. Mateiasi, M. Neagu, S. Szobotka, and O. G. Duliu, Eng Geol **103**, 119 (2009).

33. V. Cnudde and M. N. Boone, Earth Sci Rev **123**, 1 (2013).

34. V. Cnudde, B. Masschaele, M. Dierick, J. Vlassenbroeck, L. Van Hoorebeke, and P. Jacobs, Applied Geochemistry **21**, 826 (2006).

35. H. Andrä, N. Combaret, J. Dvorkin, E. Glatt, J. Han, M. Kabel, Y. Keehm, F. Krzikalla, M. Lee, C. Madonna, M. Marsh, T. Mukerji, E. H. Saenger, R. Sain, N. Saxena, S. Ricker, A. Wiegmann, and X. Zhan, Comput Geosci **50**, 25 (2013).

36. R. T. Armstrong, J. E. McClure, M. A. Berrill, M. Rücker, S. Schlüter, and S. Berg, Phys Rev E **94**, 043113 (2016).

37. R. T. Armstrong, J. E. McClure, V. Robins, Z. Liu, C. H. Arns, S. Schlüter, and S. Berg, Transp Porous Media **130**, 305 (2019).

38. J. A. White, R. I. Borja, and J. T. Fredrich, Acta Geotech (2006).

39. C. H. Arns, A. Sakellariou, T. J. Senden, A. P. Sheppard, R. M. Sok, M. A. Knackstedt, W. V. Pinczewski, and G. F. Bunn, in *SEG Technical Program Expanded Abstracts 2003* (Society of Exploration Geophysicists*, 2003*), pp. 1477–1480.

40. Y. Hou, D. Liu, T. Zhao, J. Zhou, L. Tian, X. Kou, B. Zhu, and X. Nie, Processes (2023).

41. H. Agbogun, T. A. Al, and E. M. A. Hussein, J Contam Hydrol (2013).

42. X. Liu, J. Sun, and H. Wang, Applied Geophysics **6**, 1 (2009).

43. A. Mahmoud, R. Gajbhiye, J. Li, J. Dvorkin, S. R. Hussaini, and H. S. AlMukainah, Arabian Journal of Geosciences **16**, 248 (2023).

44. L. C. Ruspini, P. E. Øren, S. Berg, S. Masalmeh, T. Bultreys, C. Taberner, T. Sorop, F. Marcelis, M. Appel, J. Freeman, and O. B. Wilson, Transp Porous Media **139**, 301 (2021).

45. N. Alqahtani, (2021).

46. M. Regaieg, T. Faisal, F. Nono, F. Pairoys, V. Fernandes, and C. Caubit, *Prediction of Relative Permeability and Fast Wettability Assessment Using Digital Rock Physics: An Operational Study on a Reservoir Sandstone* (*2023*).

47. M. Regaieg, F. Nono, T. Faisal, C. Varloteaux, and R. Rivenq, *Pore Network Simulations Coupled with Innovative Wettability Anchoring Experiment to Predict Relative Permeability of a Mixed-Wet Rock* (*2022*).

48. A. P. Teles, I. Lima, and R. T. Lopes, Micron **83**, 72 (2016).

49. P. Grangeat, (1991).

50. R. A. Ketcham and R. D. Hanna, Comput Geosci **67**, 49 (2014).

51. C. H. Arns, H. Jiang, H. Dai, I. Shikhov, N. I. Sayedakram, and J.-Y. Arns, E3S Web of Conferences (2019).

52. Q. Lin, Y. Al-Khulaifi, M. J. Blunt, and B. Bijeljic, Adv Water Resour **96**, 306 (2016).

53. A. Mehmani and M. Prodanović, Adv Water Resour **63**, 104 (2014).

54. C. Sun, J. E. McClure, P. Mostaghimi, A. L. Herring, S. Berg, and R. T. Armstrong, Geophys Res Lett **47**, e2019GL086151 (2020).

55. Y. Da Wang, L. M. Kearney, M. J. Blunt, C. Sun, K. Tang, P. Mostaghimi, and R. T. Armstrong, Adv Colloid Interface Sci **326**, 103122 (2024).

56. H. Andrä, H. Andrä, N. Combaret, N. Combaret, J. Dvorkin, J. Dvorkin, E. Glatt, E. Glatt, J. Han, J. Han, M. Kabel, M. Kabel, Y. Keehm, Y. Keehm, F. Krzikalla, F. Krzikalla, M. Lee, M. Lee, C. Madonna, C. Madonna, M. Marsh, M. Marsh, T. Mukerji, T. Mukerji, E. H. Saenger, E. H. Saenger, R. Sain, R. Sain, N. Saxena, N. Saxena, S. L. Ricker, S. Ricker, S. Ricker, S. Ricker, A. Wiegmann, A. Wiegmann, X. Zhan, and X. Zhan, Comput Geosci (2013).

57. S. Higgs, Y. Da Wang, C. Sun, J. Ennis-King, S. J. Jackson, R. T. Armstrong, and P. Mostaghimi, Int J Hydrogen Energy **47**, 13062 (2022).

58. M. Boon and H. Hajibeygi, Sci Rep **12**, 14604 (2022).

59. Fabrice Pairoys, L. R. Cyril Caubit, Nepesov, Nicolas Agenet, Danielczick, and Franck Nono, in *Society of Core Analyst* (*2023*).

60. Y. Niu, S. J. Jackson, N. Alqahtani, P. Mostaghimi, and R. T. Armstrong, Transp Porous Media **144**, 825 (2022).

61. Y. Da Wang, M. J. Blunt, R. T. Armstrong, and P. Mostaghimi, Earth Sci Rev **215**, 103555 (2021).

62. J. Zhang, Y. Tang, D. He, P. Sun, and X. Zou, Appl Clay Sci **196**, 105758 (2020).

63. M. ; L. Kampschulte A. C.; Sender J.; Litzlbauer H. D.; Althöhn U.; Schwab J. D.; Alejandre-Lafont E.; Martels G.; Krombach G. A., RöFo - Fortschritte auf dem Gebiet der Röntgenstrahlen und der bildgebenden Verfahren **188**, 146 (2016).

64. M. Garum, P. W. J. Glover, P. Lorinczi, G. Scott, and A. Hassanpour, Energy & Fuels **35**, 702 (2021).

65. K. Yu, K. Zhao, and Y. Ju, Appl Clay Sci **218**, 106430 (2022).

66. Y. Sun, Y. Zhao, and L. Yuan, Microporous and Mesoporous Materials **258**, 8 (2018).

67. S. Wu, X. Zhai, Z. Yang, H. Bale, Y. Hong, J. Cui, S. Pan, and S. Lin, Mar Pet Geol **107**, 397 (2019).

68. A. Singhal, J. C. Grande, and Y. Zhou, Micros Today **21**, 16 (2013).

69. Y. Wang, A. Alzaben, C. H. Arns, and S. Sun, Comput Geosci **150**, 104712 (2021).

70. M. S. Jouini and N. Keskes, Appl Math Model **41**, 562 (2017).

71. J. G. Maas, A. Hebing, and P. G. Bv, (2013).

72. T. Astsauri, M. Habiburrahman, A. F. Ibrahim, and Y. Wang, Sci Rep (2024).

73. A. Singh, K. Regenauer-Lieb, S. D. C. Walsh, R. T. Armstrong, J. J. M. van Griethuysen, and P. Mostaghimi, Geophys Res Lett (2020).

74. S. Sadeghnejad, M. Reinhardt, F. Enzmann, P. Arnold, B. Brandstätter, H. Ott, F. Wilde, S. Hupfer, T. Schäfer, and M. Kersten, Adv Water Resour **179**, 104501 (2023).

75. X. Wang and M. Cai, Rock Mech Rock Eng **53**, 1053 (2020).

76. S. Latham, T. Varslot, and A. Sheppard, (2008).